

## Article

# Start of Injection Influence on In-Cylinder Fuel Distribution, Engine Performance and Emission Characteristic in a RCCI Marine Engine

Alireza Kakoee <sup>1</sup>, Maciej Mikulski <sup>1,\*</sup>, Aneesh Vasudev <sup>1</sup>, Martin Axelsson <sup>2</sup>, Jari Hyvönen <sup>2</sup>,  
Mohammad Mahdi Salahi <sup>3</sup> and Amin Mahmoudzadeh Andwari <sup>3</sup>

- <sup>1</sup> Efficient Powertrain Solutions (EPS), School of Technology and Innovation, University of Vaasa, Yliopistoranta 10, FI-65200 Vaasa, Finland; alireza.kakoee@uwasa.fi (A.K.); aneesh.vasudev@uwasa.fi (A.V.)
- <sup>2</sup> Engine Research and Technology Development at Wärtsilä Marine Solutions, FI-65101 Vaasa, Finland; martin.axelsson@wartsila.com (M.A.); jari.hyvonen@wartsila.com (J.H.)
- <sup>3</sup> Machine and Vehicle Design (MVD), Materials and Mechanical Engineering, Faculty of Technology, University of Oulu, FI-90014 Oulu, Finland; mahdi.salahi@oulu.fi (M.M.S.); amin.m.andwari@oulu.fi (A.M.A.)
- \* Correspondence: maciej.mikulski@uwasa.fi

**Abstract:** Reactivity-controlled compression ignition (RCCI) is a promising new combustion technology for marine applications. It has offered the potential to achieve low NO<sub>x</sub> emissions and high thermal efficiency, which are both important considerations for marine engines. However, the performance of RCCI engines is sensitive to a number of factors, including the start of injection. This study used computational fluid dynamics (CFD) to investigate the effects of start of injection (SOI) on the performance of a marine RCCI engine. The CFD model was validated against experimental data, and the results showed that the SOI has a significant impact on the combustion process. In particular, the SOI affected the distribution of fuel and air in the combustion chamber, which in turn affected the rate of heat release and the formation of pollutants. Ten different SOIs were implemented on a validated closed-loop CFD model from 96 to 42 CAD bTDC (crank angle degree before top dead center) at six-degree intervals. A chemical kinetic mechanism of 54 species and 269 reactions tuned and used for simulation of in-cylinder combustion. The results show that in early injection, high-reactivity fuel was distributed close to the liner. This distribution was around the center of late injection angles. A homogeneity study was carried out to investigate the local equivalence ratio. It showed a more homogenous mixture in early injection until 66 CAD bTDC, after which point, earlier injection timing had no effect on homogeneity. Maximum indicated mean effective pressure (IMEP) was achieved at SOI 48 CAD bTDC, and minimum amounts of THC (total hydrocarbons) and NO<sub>x</sub> were observed with middle injection timing angles around 66 CAD bTDC.

**Keywords:** combustion; engines; RCCI; homogeneity; emissions; NO<sub>x</sub>; unburned hydrocarbons; injection timing



**Citation:** Kakoee, A.; Mikulski, M.; Vasudev, A.; Axelsson, M.; Hyvönen, J.; Salahi, M.M.; Mahmoudzadeh Andwari, A. Start of Injection Influence on In-Cylinder Fuel Distribution, Engine Performance and Emission Characteristic in a RCCI Marine Engine. *Energies* **2024**, *17*, 2370. <https://doi.org/10.3390/en17102370>

Academic Editor: Emiliano Mucchi

Received: 21 April 2024

Revised: 8 May 2024

Accepted: 9 May 2024

Published: 14 May 2024



**Copyright:** © 2024 by the authors. Licensee MDPI, Basel, Switzerland. This article is an open access article distributed under the terms and conditions of the Creative Commons Attribution (CC BY) license (<https://creativecommons.org/licenses/by/4.0/>).

## 1. Introduction

Reactivity controlled compression ignition (RCCI) is a combustion technology that combines the benefits of homogeneous charge compression ignition (HCCI) and diesel combustion. It uses a mixture of two fuels with different reactivities to achieve low NO<sub>x</sub> (Nitrogen oxides) emissions and high thermal efficiency. RCCI engines are still under development; they have shown various potentials to operate under regulatory limitations with reasonably low emissions in comparison with conventional modes of combustion [1,2].

At present, RCCI combustion offers significant potential for lowering NO<sub>x</sub> and particulate matter (PM) emissions compared to conventional combustion engines. The unique fuel blending and combustion strategies in RCCI engines have led to improved combustion control, resulting in lower peak combustion temperatures and reduced formation of NO<sub>x</sub>.

Additionally, the use of premixed fuel in the combustion chamber aids in achieving more complete fuel oxidation, minimizing PM emissions. However, RCCI engines may still face challenges in controlling unburned hydrocarbon (UHC) and carbon monoxide (CO) emissions. Addressing these challenges requires optimizing fuel injection parameters, combustion phasing, and aftertreatment systems. Recent and ongoing research and development efforts are focused on further improving emission control strategies for RCCI engines to achieve even cleaner and more efficient combustion [3–6].

In RCCI combustion mode studies, under low-load conditions and when employing a larger proportion of low-reactivity fuel, there has been an increased probability of incomplete combustion and resultant emissions of CO and UHC [7,8]. Conversely, when the engine is run at higher loads or with a greater concentration of high-reactivity fuel (HRF), there is a predisposition toward engine knocking, higher peak pressures, and elevated  $\text{NO}_x$  emissions [9–12].

Given the significance of reducing  $\text{CO}_2$  and unburned hydrocarbons (UHC), recent investigations have focused on alternative, primarily carbon-free fuels, mainly ammonia, in RCCI engines [13]. The primary challenge in using ammonia is its lower fuel reactivity compared to hydrocarbon fuels. Its higher octane number and slower flame speed may affect efficiency and performance in certain applications, causing some challenges for researchers [14]. In the context of internal combustion engines, ammonia's challenges in use have led to its use in combination with high cetane number fuels like n-heptane, methane, or hydrogen to enhance flame speed [15,16]. On the other hand, enhancing ammonia flame speed usually causes the production of higher amounts of  $\text{NO}_x$  [17]. To overcome this challenge, wet combustion has been proposed not only for  $\text{NH}_3$  blends but also for other types of fuel, such as diesel, syngas, and hydrogen [17].

Regardless of fuel types, achieving the right fuel stratification through the adoption of an appropriate injection strategy could enhance engine performance and also mitigate any undesirable outcomes. Various strategies have been suggested and evaluated to manage mixture uniformity within the combustion chamber. These included such techniques as split injection [18,19], control of injection timing parameters [20,21], and injection pressure [22].

One of the key factors that affect the performance of RCCI engines is the start of injection (SOI). SOI has a significant impact on the distribution of fuel and air in the combustion chamber due to a lack of homogeneity, which in turn affects the rate of heat release and the formation of pollutants. In recent years, several investigations have been conducted regarding RCCI combustion strategies with different fuels and various types of injection. Li et al. numerically studied the SOI timing effect in a gasoline/biodiesel-fueled RCCI engine and reported that advanced SOI timing could result in enhanced controllability for combustion start and phasing [23]. Studies on various fuel compositions have consistently revealed that delaying the SOI caused higher in-cylinder mixture reactivity and can even lead to changes in the combustion regime, whereas advanced injection results in improvements to mixture homogenization [24–26].

To improve low-load engine operation in RCCI mode, Liu et al. [6] used optical diagnostics techniques to study the impact of SOI timing of high-reactivity fuel on combustion and flame characteristics. They reported that delaying SOI could reduce ignition delay time and create a higher concentration gradient in the combustible mixture, which resulted in a higher apparent heat release rate and shorter combustion duration. They also observed from natural combustion luminosity images that later SOI timing significantly influenced the properties of flame kernels formation and propagation.

Computational fluid dynamics (CFD) are a powerful tool that can be used to investigate the effects of SOI on the performance of RCCI engines. CFD models could be used to simulate the flow of air and fuel in the combustion chamber, as well as the combustion process itself. This allows researchers to study the effects of different SOI strategies on mixture homogeneity and its effectiveness on emissions, efficiency, and other performance metrics. There have been a number of studies that have used CFD to investigate the effects of SOI on RCCI engines [26–28].

Chemical kinetic reaction mechanisms have played a crucial role in accurately simulating the complex combustion processes in internal combustion engines. In one study, a well-established 54 species and 296 reaction mechanisms were selected for use in the simulation [29]. This mechanism has been previously validated by A. Vasudev et al. [30], providing confidence in its accuracy and reliability. The validation process likely involved comparing the predicted results from the mechanism to experimental data, ensuring that it captured the important chemical reactions and species involved in the combustion process.

By utilizing a validated chemical kinetic mechanism, the simulation could provide a more realistic representation of combustion behavior and species evolution within the engine. The selected mechanism's ability to accurately predict combustion characteristics, such as ignition timing, heat release rates, and pollutant formation, enhanced the credibility and usefulness of the simulation results.

In summary, the concept of homogeneity in fuel–air mixtures has played a critical role in the performance and emission RCCI engines. RCCI, a form of dual-fuel combustion strategy, has relied on the precise control of fuel reactivity and the stratification of fuel–air mixtures to optimize combustion efficiency and reduce emissions.

In the context of RCCI engines, the degree of mixture homogeneity can be manipulated by adjusting the injection timing. This study's innovative approach lied in its focus on the local equivalence ratio ( $\phi_i$ ) to assess homogeneity. This metric provides a granular view of how well the fuels are mixed in different regions of the combustion chamber at various stages of the engine cycle. By linking  $\phi_i$  with SOI adjustments, the study determines the optimal injection timing that maximizes combustion efficiency while minimizing harmful emissions. The approach is further instrumental for building reduced-order multizone models that aim to reproduce cylinder inhomogeneity in a fast 0-dimensional framework.

## 2. Methodology

Numerical simulation methods have been conducted in this study to investigate SOI effects on fuel mixture homogeneity and its relevance to engine performance and emissions. The validation process involved comparing the simulated results of the CFD model against one experimental data obtained under medium engine load conditions. The experimental setup will be introduced later in this section.

To initialize the CFD model, a non-reactive open-loop simulation was performed inlet valve open (IVO) until the inlet valve close (IVC) to extract required data at IVC for close loop simulations. This initial step helped establish the initial flow and thermodynamic conditions within the engine. Subsequently, all other simulations were conducted in reactive mode in a closed-loop model, considering the combustion reactions and their impact on engine performance and emissions.

By comparing the simulated results against the measured data for this specific case, the accuracy and reliability of the CFD model were assessed. Parameters such as level of homogeneity, engine efficiency, indicated mean effective pressure (IMEP), exhaust gas temperature, and pollutant emissions ( $\text{NO}_x$ , UHC) were analyzed and compared with various starts of injection.

### 2.1. Experimental Setup

Table 1 presents an overview of the research engine's specifications, as observed during the test campaign. The 6L20CRDF research engine, a derivative of the Wärtsilä 20 platform, features an inline 6-cylinder dual-fuel (DF) configuration. However, some modifications have been applied to all components except the crankshaft and connecting rod.

**Table 1.** Specification of the Wärtsilä marine engine used for model identification and validation.

Displacement/Nominal Speed	8.80 L/1000 rpm
Stroke/Bore	1.4
Air System	Two-stage turbocharged (in series)
High reactivity fuel system	Common rail
Low reactivity fuel system	Low-pressure; multi-point, upstream of the intake valve
Valve train	4 valves per cylinder, fully variable hydraulic valve train
Emission System	Horiba Mexa-One (NO <sub>x</sub> , CO, THC, CO <sub>2</sub> , O <sub>2</sub> ) AVL415S (FSN-Soot)
Indicative System	AVL Indicom, Cylinder pressure transducer Kistler 6124 A, 300 bar range, 30 pC/bar sensitivity.per
Engine Control system	Speed Goat/CanApe Rapid control prototyping platform
Test fuels	ISO 8217 [31] compliant LFO/LNG (MN = 80)

To bolster the engine's automation capabilities, the SG/CANape Rapid control prototyping environment was used. This integration served to elevate the development of automation functionalities. Notably, the engine boasted a fully variable electrohydraulic valve actuation system, affording complete freedom in adjusting both valve lift and timing. The engine architecture adopted a two-stage turbocharging setup in a series configuration.

A single-needle injector was centrally positioned for direct injection of high-reactivity fuel (direct injection) in the top of the cylinder with 9 nozzle holes. The delivery of light fuel oil (LFO) was carried out in steps based on the appropriate engine crank angle. Complementing this, the engine featured a multi-point gas injection system positioned upstream of the intake valves. This was facilitated through a low-pressure solenoid valve, thus completing the RCCI mode of operation.

Throughout the test campaign, the chosen fuel combination consisted of liquified natural gas (LNG) with a methane number of approximately 80, coupled with light fuel oil serving as the high-reactivity fuel. For the application of RCCI mode, the LFO injection was characterized by short durations and early injection timings, per RCCI specifications.

The data used for validating the model consisted of detailed pressure measurements within the cylinder at different operating points. For each steady-state condition, signals were recorded continuously for 300 cycles, with a precision of 0.2 degrees of crank angle. In-cylinder pressure data was then post-processed to calculate essential combustion indicators such as the indicated mean effective pressure (IMEP) and the crank angle at which a certain percentage of mass had burned (CAX).

Low-frequency measurements involved tracking the usage of specific fuels (using a Coriolis flow meter for gaseous fuel and a gravimetric fuel balance for liquid fuel), as well as monitoring air consumption and measuring intake and exhaust pressures and temperatures. The data also included a thorough analysis of the charge's thermal properties at intake and exhaust ports, as well as component temperatures like piston top, liner, valves, and cylinder head.

## 2.2. Model Initialization and Solver Setting

Model initialization was important for accurate simulations, involving geometry creation, boundary conditions, and proper fuel properties. In this study, a closed-loop model (from inlet valve closure (IVC) to exhaust valve closure (EVO), without considering ports and valves directly in simulation) model was selected. Head, piston, and liner temperature were adjusted according to available measured data. Initial values for pressure and temperature for IVC condition were selected from intake and exhaust port specifications. A non-reactive CFD simulation, including in cylinder valve motion, has been conducted to set the IVC conditions for the reactive simulation. Simulation accuracy depended on precise

chemical kinetics, boundary setup, and turbulence models for combustion phenomena. The realistic fuel injection simulation required accurate injector modeling and careful grid control for efficiency and accuracy.

### 2.2.1. Geometry and Mesh Generation

Figure 1 displays the closed-loop model geometry at the top and bottom, dead center for the CFD simulation. The model represented an internal combustion engine with head, liner, and piston components. Initialization, boundary conditions, and solver settings were configured in Converge Studio software v3.1. Utilizing dynamic mesh generation and unstructured grids enhanced flexibility and efficiency, reducing computational demands while preserving accuracy.

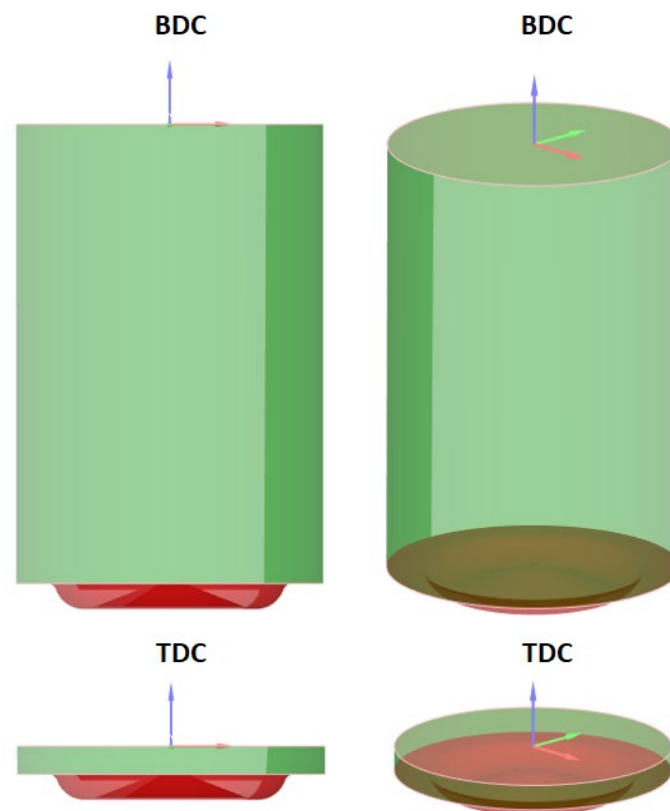


**Figure 1.** Cylinder closed-loop geometry model positioned at TDC and BDC. XYZ coordinate; x (red), y (green) and z (blue).

In the context mesh generation, the fixed embedding method was used, a technique where a stationary or non-moving mesh is generated for one part of the domain, while another mesh moves or rotates independently within it. This allows for modeling the interaction between stationary and moving components, which is essential in various engineering applications.

In this experiment, the base grid mesh size was 0.008 m and the injector's stationary components were represented by a fixed background mesh, while the moving parts needing moving meshes, the nine individual nozzles, were embedded within the background mesh. Each nozzle's mesh was generated separately from base meshes, accounting for its unique geometry and flow characteristics. The embedded mesh was dynamically linked to the background mesh, allowing for interactions between the stationary and moving components during the simulation. This method was particularly useful in modeling multi-hole injectors, where each nozzle may have had distinct spray stratifications; see Figure 2.

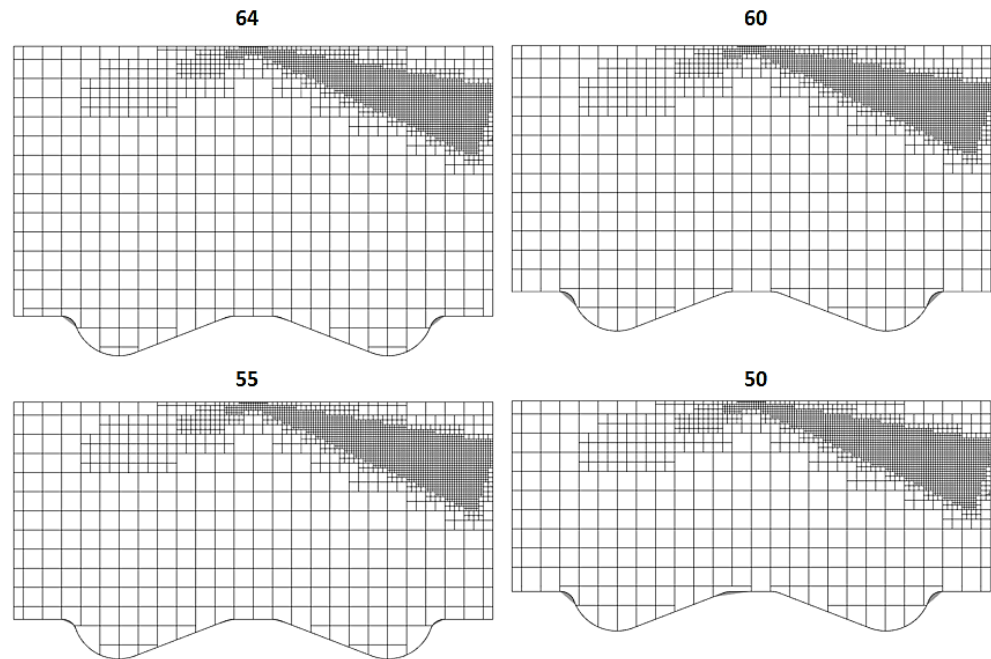


**Figure 2.** Injector-fixed embedded mesh quality depicted in four various crank angle degrees bTDC in a section through a nozzle axis.

In Figure 2, the mesh strategy has been illustrated. This figure indicates that moving mesh for whole cylinder has been used alongside with fixed embedded area for injected fuel spray cloud. The mesh quality was examined at four different piston positions, specifically at 64°, 60°, 55°, and 50° CAD bTDC (crank angle degree before top dead center).

Mesh sensitivity analysis was conducted with three different meshes of 0.002 m, 0.004 m and 0.008 m, respectively. Figure 3 illustrates the cylinder pressure for three selected mesh sizes. Since a mid-load case was selected for mesh sensitivity, the values are depicted in normalized form to consider confidentiality issues. Finer mesh and moderate, 0.002 m and 0.004 m, shown closer results; 0.008 also predicted pressure with the same trend and also the same pressure rise rate quantity. With using a high-performance computer (HPC) cluster to run the simulations with 256 CPU in use, the 0.008 m mesh took about 1088 s. The simulation run times were 1447 s and 4831 s for 0.004 m and 0.002 m mesh sizes, respectively.

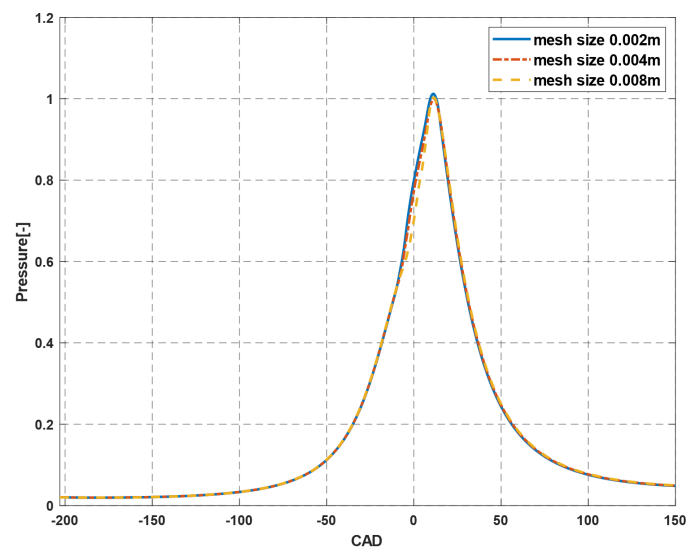


**Figure 3.** Pressure rise rate simulated with medium load data engine in various mesh sizes, normalized by maximum pressure in 0.008 m case.

### 2.2.2. Chemical Kinetic Mechanism and Liquid Fuel Properties

In the actual engine setup, LFO was utilized as the highly reactive fuel of choice. To accurately model LFO combustion, a chemical mechanism that closely represents its properties was selected. The SK54 mechanism, consisting of 54 species and 296 reactions, was chosen for this simulation. Yao et al. [29] introduced this mechanism in 2017, and it has proven to be well suited for marine engine applications, especially in large-bore setups [32]. Aneesh Vasudev conducted a comprehensive validation of the SK54 mechanism against experimental data using a multiple zone model (MZM) approach simulation, ensuring its reliability [32]. Moreover, the SK54 mechanism was effectively used in a MZM combustion simulation coupled with GT-Power by A. Kakooe et al. [33]. Although the SK54 mechanism itself does not include  $\text{NO}_x$  emission reactions, Converge Studio v3.1 as simulation software possessed the capability to incorporate it, based on the extended Zel'dovich mechanism to predict  $\text{NO}_x$  production during combustion; soot emission predictions are also possible with simulation software.  $\text{C}_2\text{H}_2$  was chosen as the primary soot precursor in this simulation. This addition enabled a more comprehensive analysis of the engine's pollutant emissions [34,35]. In the context of combustion modeling and injection simulations, parcel modeling is a powerful approach to accurately represent the behavior of individual fuel droplets. In the SK54 mechanism, n-dodecane ( $\text{NC}_{12}\text{H}_{26}$ ) was chosen as the high-reactivity fuel injected into the cylinder through the injector.

### 2.2.3. Combustion Modeling and Turbulence

In the combustion modeling process, several key decisions were made to accurately represent combustion behavior. The chemistry solver was activated from  $-75$  to  $140$  CAD aTDC to encompass the relevant combustion phases. To achieve high-fidelity results, the SAGE detailed chemistry solver was selected, employing a temperature resolution of  $2$  K and an analytical Jacobian method. CVODES with a dense solver was applied for this combustion modeling, which involved fewer than  $100$  species, providing an efficient yet accurate solution. Adaptive zoning with a  $5$  K temperature bin was chosen to enhance simulation accuracy, and the dimension of adaptive zoning was automatically calculated for optimal performance.

For turbulence modeling in the Reynolds-averaged Navier–Stokes (RANS) framework, the re-normalization group (RNG)  $k$ - $\epsilon$  model was chosen. This model is known for its improved accuracy in predicting complex turbulent flows. To account for wall interactions, the turbulence modeling configuration considered Von Karman's constant of  $0.42$  and a law of the wall parameter of  $5.5$ . The O'Rourke and Amsden model were employed for wall heat transfer modeling, while the standard wall function was applied for near-wall treatment, providing robust and efficient predictions of flow characteristics near the boundaries.

In the RANS system of equations, specific constants were selected to enhance the turbulence modeling accuracy. A value of  $0.0845$  was chosen for  $C_\mu$ , while  $C_{\epsilon 1}$ ,  $C_{\epsilon 2}$ , and  $C_{\epsilon 3}$  were set to  $1.42$ ,  $1.68$ , and  $-1$ , respectively. These constants played a critical role in determining the turbulent dissipation and eddy viscosity within the flow field. To ensure appropriate thermal modeling, the reciprocal of turbulent kinetic energy (tke) and the turbulent kinetic energy dissipation rate ( $\epsilon$ ), Prandtl numbers were both adjusted to  $1.39$ . Additionally,  $\beta$  was set to  $0.012$  and  $\eta_0$  was set at  $4.38$ , enabling the model to accurately account for turbulence and thermal effects throughout the simulation domain.

The O'Rourke model was utilized to account for turbulent dispersion, ensuring an accurate representation of the spray dispersion in the combustion process. The Frosslig model was chosen to describe the evaporation of liquid parcels, accounting for the vaporization process during spray injection.

Dynamic drop drag was employed for drag force calculation, using three dynamic drag variables with values of  $0.083333$ ,  $10$ , and  $8$ , respectively, to accurately capture the interactions between the liquid droplets and the surrounding gas. The Rayleigh–Taylor (RT) model was selected, incorporating a chi-squared distribution to describe the breakup

process accurately. Additionally, child parcel creation was chosen for the Kelvin–Helmholtz (KH) model, along with specific required constants.

In the model simulation, the liquid injection temperature was approximately 340 K, and the injector rail pressure was set at 1880 bar. Leveraging the known data about the injector, a rate shape was developed and applied to all nozzle holes uniformly. Injection duration in degrees, injection mass in kilograms, and start of injection are precisely specified for each case study model. Finally, in the parcel configuration regarding the mesh size, appropriate parcel quantities were selected.

### 2.3. Operating Points, Boundary Conditions and Initial Values

In the simulation, the head and liner boundaries were stationary, representing fixed positions, while the piston was a moving boundary. The temperature boundary used the law of the wall to assess temperature near walls, considering thermal behavior. Assuming negligible roughness and a roughness constant refined the law of the wall treatment, simplifying wall effects modeling.

For wall heat transfer modeling, the O'Rourke and Amsden [14] model was selected, chosen for reliable fluid–solid heat exchange representation. Turbulent flow properties utilize the Neumann condition for turbulent kinetic energy, ensuring zero gradient normal to the boundary, and the law of the wall was selected for turbulent dissipation boundary condition (EPS).

In the closed-loop simulation, the entire cylinder was set as the simulation region. For the RCCI simulation, the initial conditions at IVC condition were carefully defined as explained before. The available species were set to O<sub>2</sub> and N<sub>2</sub>, representing air, while an appropriate combination of CH<sub>4</sub> and C<sub>2</sub>H<sub>6</sub> was chosen to serve as the LRF. Although residual gases are present at IVC, their amounts were assumed to be negligible.

Table 2 presents the detailed specifications of a medium load case study, including boundary conditions, initial values, and engine operating conditions. The data were presented with respect to a reference 25% load conventional dual-fuel calibration on the engine shown as ref. Additionally, the table provided useful information about the initial cylinder composition, which represents the low-reactivity fuel concentration at IVC. For consistency, the engine speed was set at 1000 rpm this case and proper optimization simulations, while the engine operated at 50% of load. In this table, Y denotes the mass fraction.

**Table 2.** Engine operating points, boundary conditions and initial values for three low, mid and high load cases.

	Specifications/Case	B (Mid Load)
Operating Points	Speed (rpm)	1000
	Injected mass (mg)	ref – 28
	SOI (CAD bTDC)	ref + 31
	Injection duration (CAD)	2.5
Boundary Conditions	T_piston (k)	ref – 84
	T_Head (k)	ref – 15
	T_liner (k)	ref – 5
	T_wall_exh_port	ref – 3.4
	T_wall_int_port	ref – 2.4
	P_exh_port	ref + 1.6
	P_int_port	ref + 1.6
	T_exh_port	ref – 31.1
T_int_port	ref + 6.5	

Table 2. Cont.

	Specifications/Case	B (Mid Load)
Initial Values	T <sub>ivc</sub> (k)	ref + 14.8
	P <sub>ivc</sub> (bar)	ref + 1.92
	Y <sub>N<sub>2</sub></sub>	0.7531
	Y <sub>O<sub>2</sub></sub>	0.2288
	Y <sub>CH<sub>4</sub></sub>	0.0168
	Y <sub>C<sub>2</sub>H<sub>6</sub></sub>	0.0013

### 3. Results and Discussion

The results of the current study have been organized into three distinct parts, each offering different insights into the performance of the simulated engine models. In the first part, the outcomes of the validation case study (presented in Table 2) were thoroughly compared to experimental results. This comparison served as a validation step, confirming the accuracy and reliability of the simulated models in terms of various mentioned specifications. By demonstrating close agreement between the simulated and experimental data, the validity of the simulation approach was established.

In the second part, the results of various injection timing strategies were comprehensively analyzed to showcase their effectiveness on fuel distribution, engine outputs, combustion characteristics, and emission levels. This thorough explanation provided a deeper understanding of how varying injection timings and homogeneity level impact the overall engine performance and pollutant formation, guiding the selection of optimal injection strategies. Lastly, the third part, visualization, focused on flow based on engine outputs and emissions.

#### 3.1. Model Validation and Results

The validation process in this study involved comparing the simulated results to the available experimental data for a mid-load case study; see Table 2. Various crucial parameters were examined during the validation procedure. In particular, the in-cylinder thermodynamic properties, such as pressure and heat release rate (HRR), were chosen. To assess the accuracy of the simulation, graphical comparisons were made between the simulated and experimental pressure and HRR data.

In Figure 4, a detailed comparison is presented between the in-cylinder pressure and HRR. The results indicated a good level of compatibility between the simulated and experimental data. Both the pressure and HRR in the simulation closely follow the experimental curves, showcasing the accuracy of the simulation model in capturing the combustion characteristics. Pressure has been normalized with experimental maximum pressure and HRR with total fuel energy. The peak pressure was predicted with an absolute error of +4.2 bar, while the position of peak pressure was within 1 CAD, both within 2.5% accuracy ( $\frac{P_{max\ sim}}{P_{max\ exp}} = 1.025$ ), indicating the good precision of the simulation results in predicting critical engine performance parameters. Moreover, root mean square (RMS) error of predicted pressure with experimental one was about 1.15 bar. This error for HRR was 0.0476 kJ/s.

It is worth noting that, in order to achieve a highly compatible pressure curve and heat release rate, the chemical kinetic mechanism utilized in this study was carefully tuned. Through this tuning process, the new mechanism demonstrated improved accuracy in predicting both thermodynamic properties and emission outputs, as well as engine power specifications. The key advantage of this tuned mechanism lay in the use of a tuning parameter at the IVC temperature. With this tuned mechanism, only a minimal below 1% increment in IVC temperature was required to calibrate the simulation case. In contrast, the original mechanism necessitated a much higher increment, typically ranging from 8 to 10 percent [33].

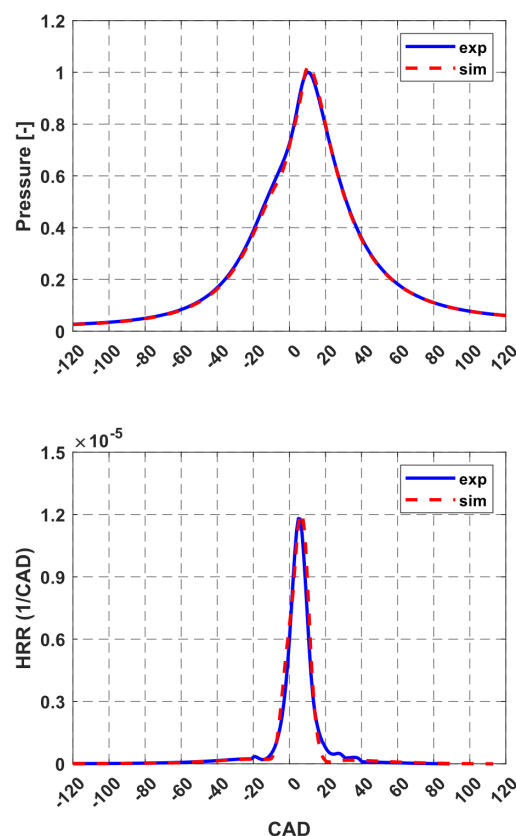


**Figure 4.** In-Cylinder pressure (normalized by experimental peak pressure) and heat release rate (Normalized by total fuel energy), experimental and simulation comparison.

The heat release profile is depicted in Figure 4, for both experiment and simulation. The ratio of specific heats,  $\gamma$ , used in the postprocessing routine to obtain heat release from the in-cylinder pressure trace is also shown in this figure. Cumulative heat release (CHR), shown in Figure 5, RMS error calculated as 0.602 kJ. Characterizing the heat release profile by CAX, which indicated the crank angle at which X percentage of the total fuel energy was released, CA10 (start of combustion) was predicted with an accuracy of 1 CAD while CA50 within 0.2 CAD. Furthermore, the error in combustion duration, i.e., CA10–90, was less than 2CAD. An additional quantity useful in fuel consumption and power output management was net heat released (NHR). This quantity was estimated with an absolute error of 0.84 kJ, resulting in a deviation of around 2.8% ( $\frac{NHR_{sim}}{NHR_{exp}} = 1.028$ ), from the experimental results.

In this study, the engine power output was assessed by comparing the indicated power, which was calculated based on the indicated mean effective pressure (IMEP). The absolute error in indicated power was +3 kW, which translates to a relative error of 2.3%. IMEP, a critical parameter in internal combustion engines, provided valuable insights into the average pressure exerted on the piston during the power stroke. This quantity was obtained with an absolute error of  $-0.4$  bar.

In the simulation study, an essential aspect was the agreement in predicting emissions when compared to experimental data. Figure 6 provides a comparison of indicated emissions of  $\text{NO}_x$  and total hydrocarbons (THC) normalized to their respective experimental measurement. While THC emissions were predicted with some differences in quantity, the magnitudes of this emission type remain within the same order. The simulation demonstrated an ability to reasonably predict THC emissions, though slight variations were observed. Similarly,  $\text{NO}_x$  emissions were predicted in approximately the same amounts between the simulation and experimental data. For instance, indicated  $\text{NO}_x$  emissions were predicted within a relative error of 1%, which demonstrated the consistency between the simulated and experimental emission performance parameters.

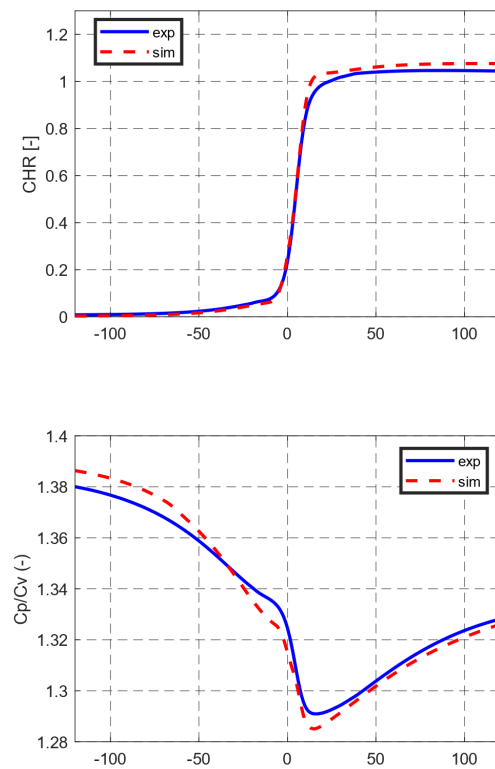


**Figure 5.** Cumulative heat release and specific heat ratio, compared for experimental and simulation cases.

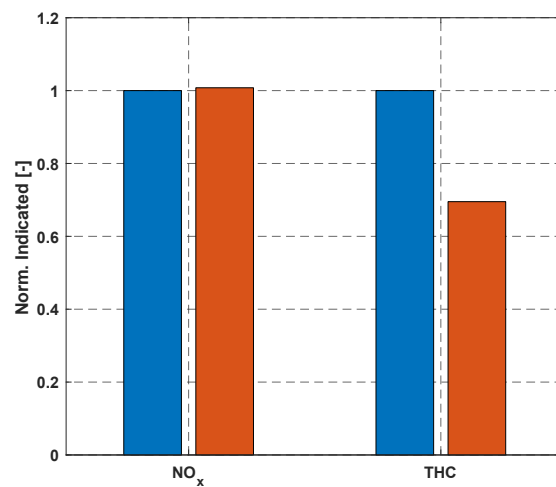


**Figure 6.** Comparison of indicated emissions ( $\text{NO}_x$  and THC) in simulations and measured, normalized to measurement data.

### 3.2. Injection Timing Effectiveness

As previously mentioned, this study investigated the impact of injection timing on various engine related specifications. A set of 10 comprehensive case studies was selected to explore the influences of varying injection timings on previously mentioned specifications.

Initially, the study delved into the influence of injection timing on the in-cylinder pressure curve, as depicted in Figure 7. Notably, the study revealed a stable trend in which the maximum pressure experienced an incremental increase with a progressively delayed start of injection. However, this upward trajectory encountered a pivotal point at approximately 54 CAD bTDC, beyond which the maximum pressure underwent a decline. This nuanced interplay between injection timing and its corresponding effects

on the engine's critical characteristic of maximum pressure is also portrayed in Figure 7. These effectiveness of injection timing also has been reported in a gasoline/biodiesel RCCI engine modeling by Li, J. et al., [23]. Nazemi, M. and Shahbakhti, M. 2016, also observed same effectiveness of injection timing on pressure peak point and curve [26]. Figure 7 also illustrates a reduction in maximum pressure ( $P_{max}$ ) when the SOI was too late, indicating incomplete combustion within the cylinder. This trend has also been observed in a numerical analysis of a heavy-duty RCCI engine, where delaying SOI led to a decrease in the pressure peak in too-late injections [36].

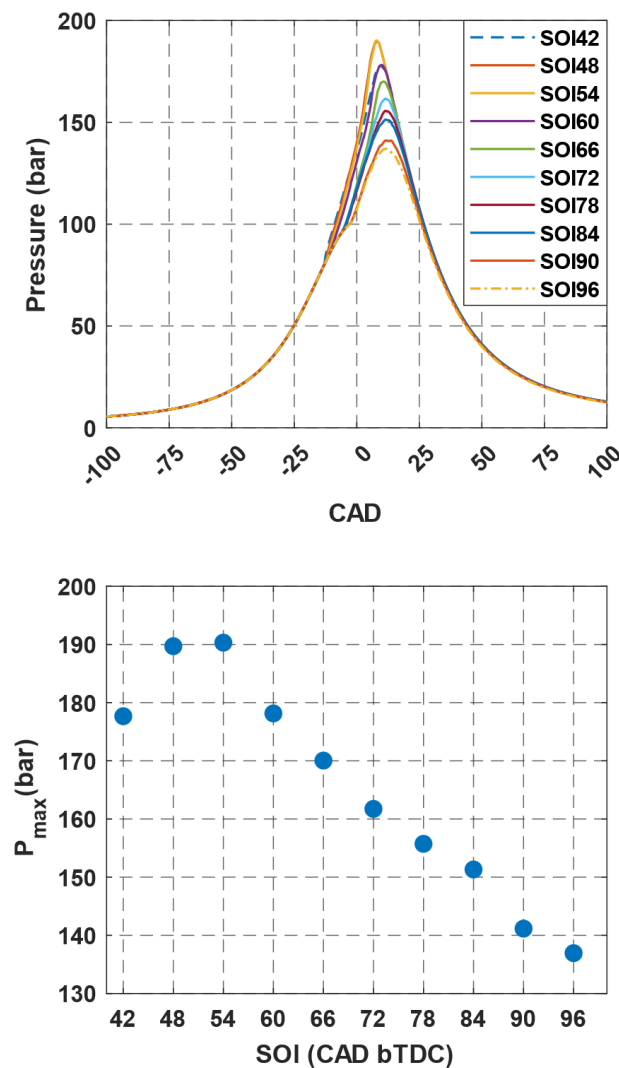


**Figure 7.** In-cylinder pressure curve and maximum pressure for various injection timing simulations.

Note that peak pressure rise rate (PRR) followed a similar trend as  $P_{max}$ . Importantly, however, the PRR did not exceed 4 bar/CAD for the given load point, regardless of the SOI, and was well in line with the engine durability limits (10 bar/CAD).

Building upon the preceding investigations, it became evident that injection timing exerted a notable influence on another critical parameter IMEP which directly correlates with engine power output. The investigation into the effects of injection timing on engine power output realized through IMEP analysis. This quantitative assessment has been visually presented in a graph, elucidated the impact of varying injection timings on engine performance.

Figure 8 depicts this influence, revealing that the maximum IMEP was prominently observed at 48 CAD bTDC. This observation aligned seamlessly with the previously es-

established trend, where the maximum pressure was also attained with the same SOI. This trend of IMEP that seemed to increase from too-late injection to middle injection angles and then decreased also observed in M.Nazemi simulation study [26]. The main reason for this trend was related to in-cylinder pressure curve that directly affected by combustion duration increase [36].

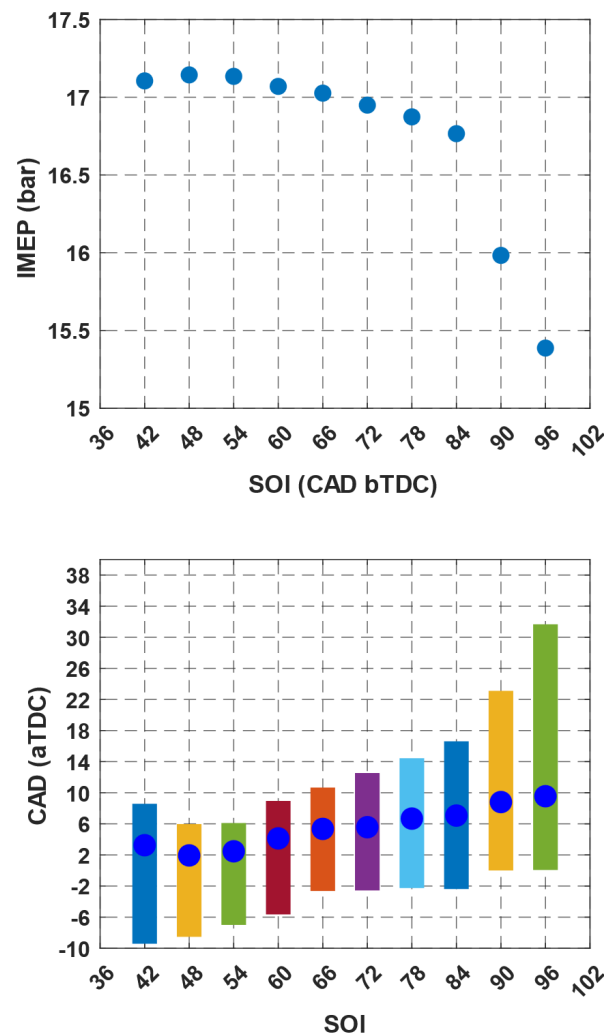


**Figure 8.** Indicated mean effective pressure (IMEP) upper graph and combustion phasing, bottom graph for various SOI.

The lower graph in Figure 8 provides a visual representation of combustion phasing across the spectrum of case studies. Each bar chart within this graph corresponds to burn duration (BD), specifically the time span between CA10 and CA90.

Taking a closer look at the scenario where the SOI was set at 48 CAD bTDC, a distinct pattern emerged. In this instance, combustion was initiated at approximately  $-7$  CAD aTDC, with its CA50 occurring around 2.2 CAD aTDC. Notably, this configuration, which yielded the highest IMEP, was characterized by a burn duration of roughly 13.5 CAD. Deliberate adjustments in SOI timings led to corresponding shifts in combustion initiation. For example, a delayed SOI resulted in an advancement of combustion start. End of combustion also advanced from 96 to 48 CAD of SOI, where it was delayed at 42 CAD of SOI, as shown in Figure 8.

An interesting pattern emerged from the study's results, particularly when the SOI was set at 90 CAD bTDC. In this case, there was a noticeable and significant drop in IMEP and a sharp increase in BD. When SOI was at 96 CAD, the duration of combustion deviated

from the expected pattern shown in Figure 8 and unexpectedly increased. In compression ignition engines, especially RCCI engines, too-early injection causes fuel blends at lower temperatures. With a lower rich zone of fuel near TDC, a delay is caused at the start of combustion, with lower ignition temperatures, which leads to lower flame speeds in RCCI engines.

In the literature, advanced in CA10 as start of combustion was also reported by M.Nazemi [26]. The inverse trend has occurred in combustion duration from 54 CAD bTDC SOI to 60 reported by Jafari, B. et al. in another research [36]. The main reason for decreasing burn duration when changing SOI from 42 to 60 can be related to CA50, when it was closer to TDC, which caused higher flame speed and shorter burn duration [36].

For a deeper insight into the details, the blue circle on the bottom graph of Figure 8 marks the CA50 point. Another result was that as the injection timing moved towards later moments, CA50 occurred closer to the end of combustion. This subtle connection had an impact on emissions, particularly unburned hydrocarbons. Among the injection timing strategies, those in the middle range shown a better match of CA50, which was different from both the early and late injection methods. The obtained results for CA50 agreed with previous studies in too-late injection examinations [36] and for early and middle injection timing, as reported by Nazemi, M. et al. [26].

Figure 9 serves as a visual representation, presenting the indicated  $\text{NO}_x$  and THC levels across different case studies. It is imperative to note that these calculations pertain to a single cylinder, and their practical implications in an actual engine would necessitate scaling to account for the number of cylinders involved.

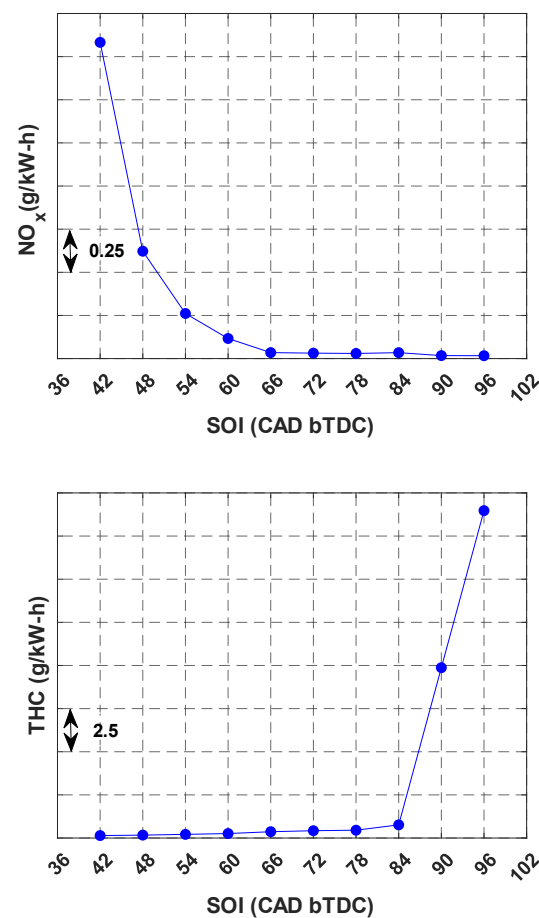
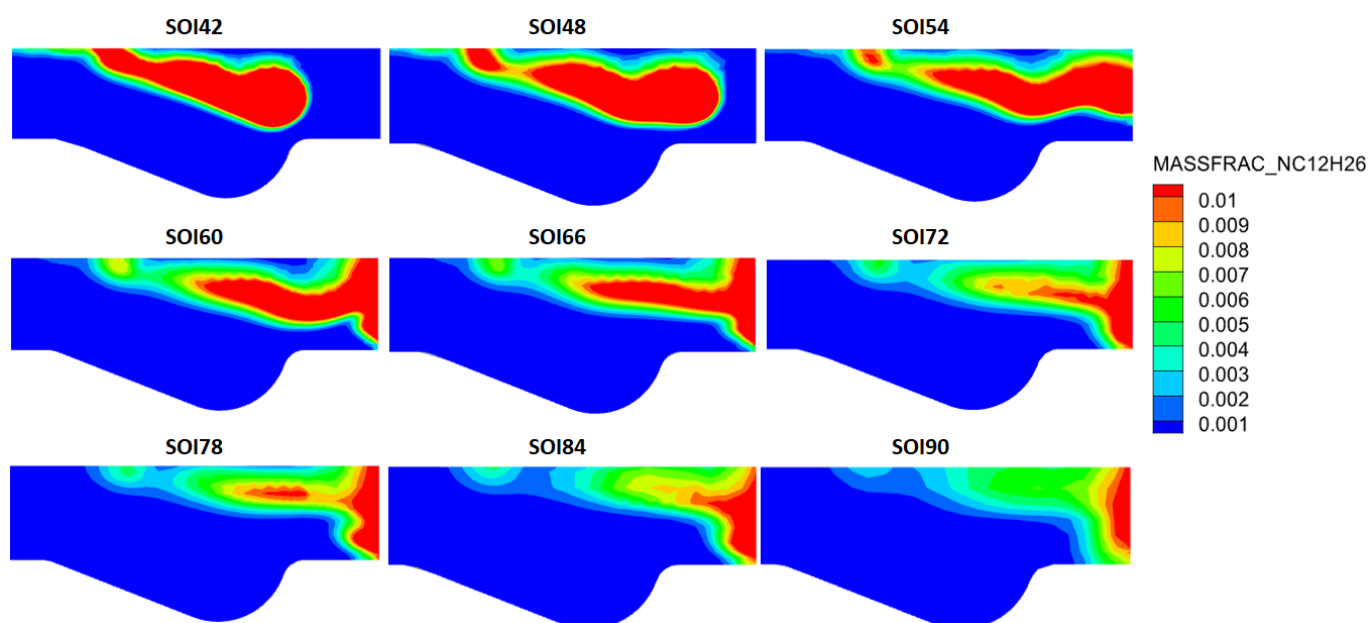


Figure 9.  $\text{NO}_x$  and total hydrocarbons (THC) in various selected SOIs.

The correlation between nitrogen-related reactions and elevated temperatures emerged as a critical factor. In the context of late injection strategies, characterized by heightened

in-cylinder temperatures, a notable surge in  $\text{NO}_x$  emissions was observed; see Figure 9. Simultaneously, the intensified thermal conditions prevalent in late injection scenarios facilitated a more thorough combustion of hydrocarbons, ultimately resulting in a reduction of THC emissions; see Figure 9. This intriguing interplay between combustion temperature, emission types, and injection timing underscore the multifaceted nature of combustion dynamics.

An examination of the output results yielded valuable insights, primarily centered around the consumption of HRF. Notably, HRF began to be consumed from approximately 16 CAD bTDC across all 10 cases. In light of this, Figure 10 presented contour depiction of  $\text{NC}_{12}\text{H}_{26}$  mass fraction for the nine distinct cases at 16 CAD bTDC. This visualization served as a dynamic window into the intricate behavior of HRF within the combustion chamber. Particularly noticeable was the discernible trend between the various injection timings and their respective HRF distribution patterns.



**Figure 10.** Mass fraction of high-reactivity fuel at 16 CAD bTDC with various start of injection angles.

In scenarios characterized by late injection strategies, the distribution of HRF predominantly gravitated toward zones proximate to the center of the combustion chamber. In contrast, the distribution pattern of early injection strategies exhibited closer proximity to the cylinder liner. This intriguing divergence in distribution, as showcased in Figure 10, underscored the critical role that injection timing plays in shaping the spatial behavior of HRF within the combustion chamber.

The visualization of this distribution has been effectively presented in Figure 11, offered a clear depiction of the percentage distribution of HRF across the cylinder bore under various start of injection conditions. This 3D illustrative graph provided a comprehensive insight into impact of SOI on the spatial distribution of HRF within the cylinder.

As has been observed along the bore axis, particularly in cases of late injection, a higher concentration of fuel was positioned closer to the center, as indicated by the prominent peak on the graph; see Figure 11. Conversely, when examining the trajectory from later to earlier SOI values, a shift in HRF distribution towards the liner was evident. This observation also be interpreted when considering the liner line (at bore), revealed a consistent increase in the HRF content with the progression from late to early injection timings. This detailed analysis contributed to a more profound understanding of dynamics at play, shaded light on the strategic importance of SOI in optimizing fuel distribution and combustion efficiency. It

should be noted that percentages were at each point of cylinder radii those cumulatively becomes 100%.

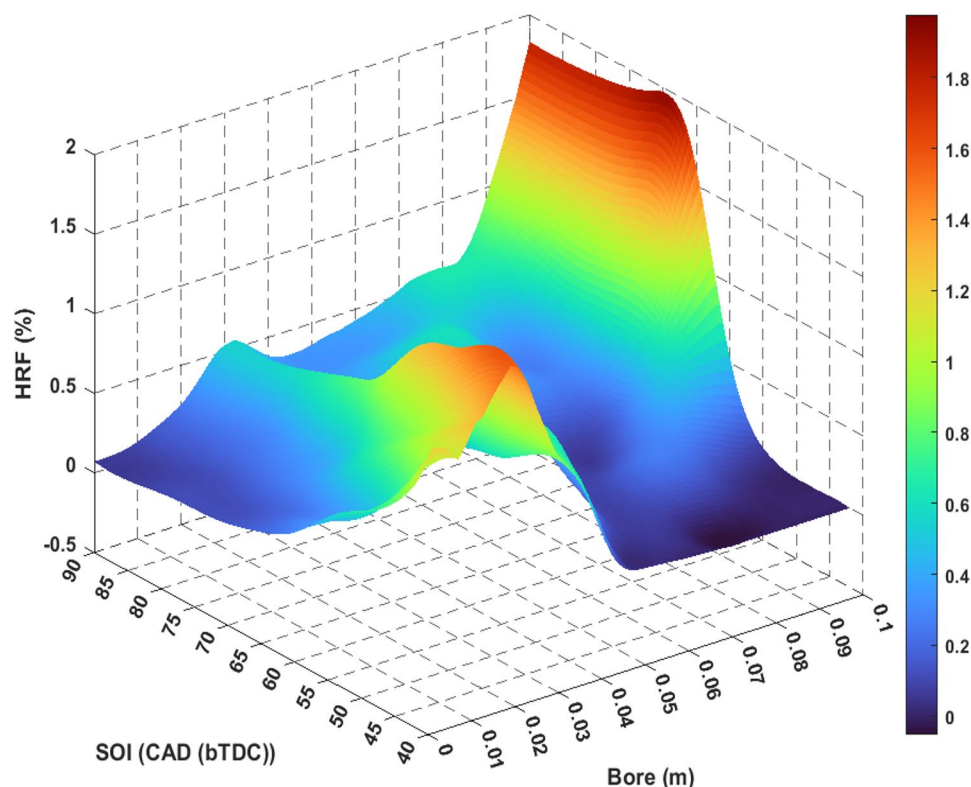


**Figure 11.** HRF distribution alongside the cylinder radii in various start of injection.

A deeper and more detailed understanding of fuel distribution is captured in Figure 12, which presents a distinct analysis of the HRF distribution across the cylinder bore. The distribution insights are effectively portrayed through a series of bar charts, which offer information about the percentage distribution of HRF across different radii within the cylinder. The cylinder has been segmented into 10 distinct zones to facilitate a nuanced examination.

The bar charts provide illuminating trends. In instances of late injection, a notable concentration of fuel was observed within the central zones of the cylinder, shown also in graph form in Figure 12. Specifically, for SOI values of 42, 48, and 54 CAD bTDC, about 65% or more of the fuel was allocated to these central zones.

As progress moved to SO I60, the distribution pattern shifted, with the majority of fuel now distributed across zones 2 to 6. In the case of SO I66, 72, and 78, despite more than a quarter of the fuel being positioned closer to the liner, the core portion of the distribution was also allocated to middle positioned zones.

In the final two cases, SO I84 and 90, a substantial shift occurred, with over 60% of the fuel now being localized within the last four zones. This variation underscored the dynamic nature of fuel distribution under different injection timings.

In fact, one of the main reasons that HRF was injected at an early crank angle degree in RCCI engines was to prepare an acceptably homogenous mixture. As it was explained previously, homogeneity was effective in various engine specifications such as combustion quality, engine power output emissions, and knocking [37–40]. In this research, the impact of SOI on homogeneity was also thoroughly investigated. Figure 13 provides a visual representation of the normal distribution of local equivalence ratios ( $\phi_i$ ) at 66 degrees CAD bTDC of SOI. These  $\phi_i$  values were computed based on cell data, representing the equivalence ratio at the center of each cell within the computational domain at 16 degrees CAD bTDC. Within this graph, the peak point (x axis) corresponds to the mean value

of  $\phi_i$ . This graphical representation underscores that a closer distribution around this central point signifies a heightened degree of homogeneity across the entire combustion volume. Conversely, the zero points on the diagram pinpointed areas where either no HRF or exceedingly minute quantities of HRF were present in the mixture, offering insights into the interplay between SOI and homogeneity.

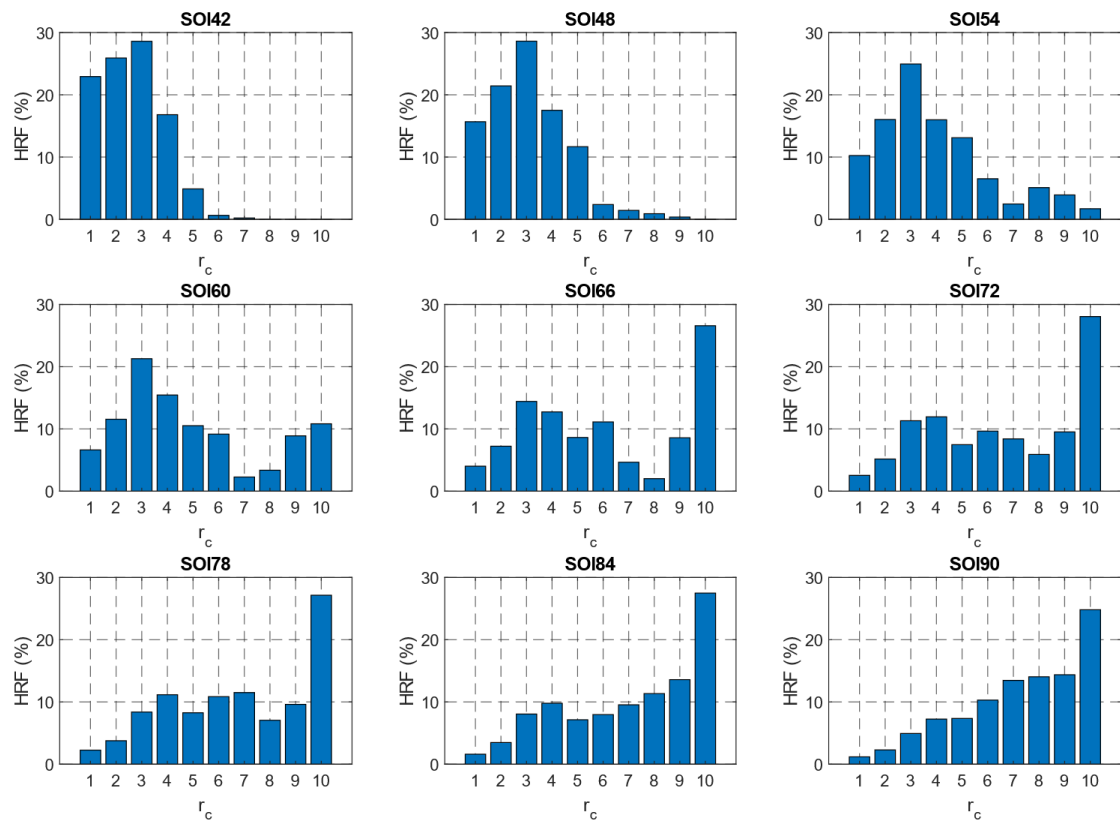


Figure 12. In-cylinder fuel distribution alongside cylinder radii divided to 10 equal zones.

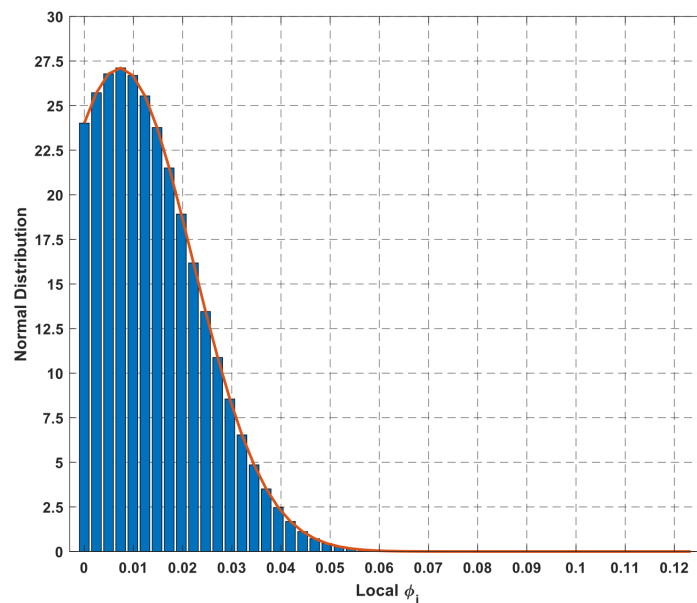
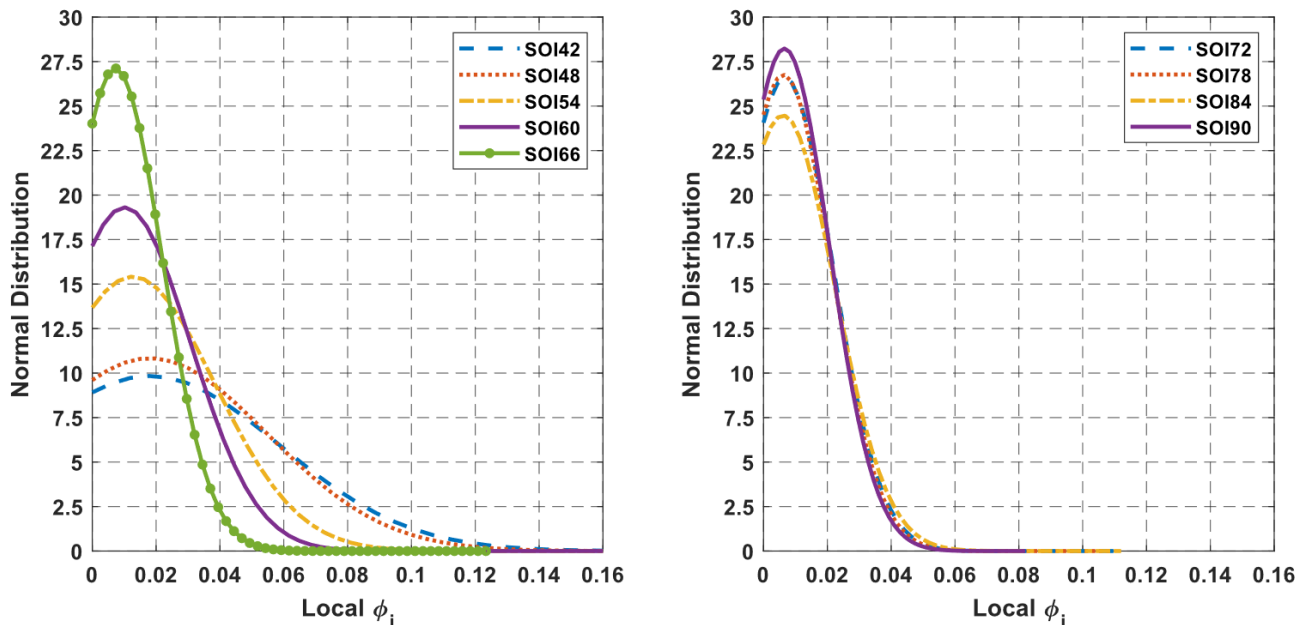


Figure 13. Normal distribution of local equivalence ratio at 16 CAD bTDC for SOI = 66 CAD bTDC.

It should be noted that local equivalence ratio  $\phi_i$ , in this study is different from actual or total equivalence ratio,  $\phi$ . In this study,  $\phi_i$  was calculated considering the amount of fuel in each specific computational cell divided by total available air, while normalizing the sum of all instances to total  $\phi$ . According to this assumption,  $\phi_i$  obtained in the order of  $10^{-2}$ .

Considering the above description of circumstances of the homogeneity study, effects of various injection timing on fuel air homogeneity have been illustrated in Figure 14. The figure divided into two parts, with the left side depicting the normal distribution of local equivalence ratios for SOI at 42, 48, 54, 60, and 66 CAD bTDC, all measured at 16 CAD bTDC piston position.



**Figure 14.** Normal distribution of local equivalence ratio for all studied injection timings at 16 CAD bTDC.

As anticipated, late injection, exemplified by SOI 42, exhibited a lower degree of homogeneity. This suggests that HRF was distributed with varying concentrations within the cylinder volume. Transitioning from late to early injection timings, there was a noticeable increase in homogeneity, marked by a narrower distribution, until SOI 66. However, beyond SOI 66, including injection timings like SOI 72, 78, 84, and 90, the level of homogeneity remained relatively unchanged, as observed in the right part of Figure 14. This shift indicated that HRF reached the cylinder liner, rendering earlier injection timings less effective in improving homogeneity.

While earlier injection timings resulted in a more homogenous fuel–air mixture in the cylinder, they also led to a higher number of cells devoid of HRF fuels. Consequently, it can be inferred that the most suitable conditions for achieving a higher level of homogeneity can occur at approximately late injection timings, where HRF didn't come into contact with the cylinder liner, but increasing level of homogeneity at late injection was the main issue.

### 3.3. Flow and Species Visualization

The flow and species visualization in this study comprised various components. Initially, to depict in-cylinder temperature zones, a specific CAD near CA50 was chosen for all cases. In Figure 15's contour representation, for SOI 42, high-temperature zones were primarily located near the center of the cylinder. Notably, as SOI was advanced from 42 CAD to earlier timings, the high-temperature zone gradually shifted toward the cylinder liner. This phenomenon was closely related to the distribution of HRF, with higher temperature zones aligning with rich regions of HRF. Among all cases depicted in Figure 15, SOI 66 showed better conditions in temperature distribution at CA50 and also allocated a

moderate in cylinder temperature. More uniform temperature distribution could also be related to higher degree of mixture homogeneity that was explained in Figure 14.

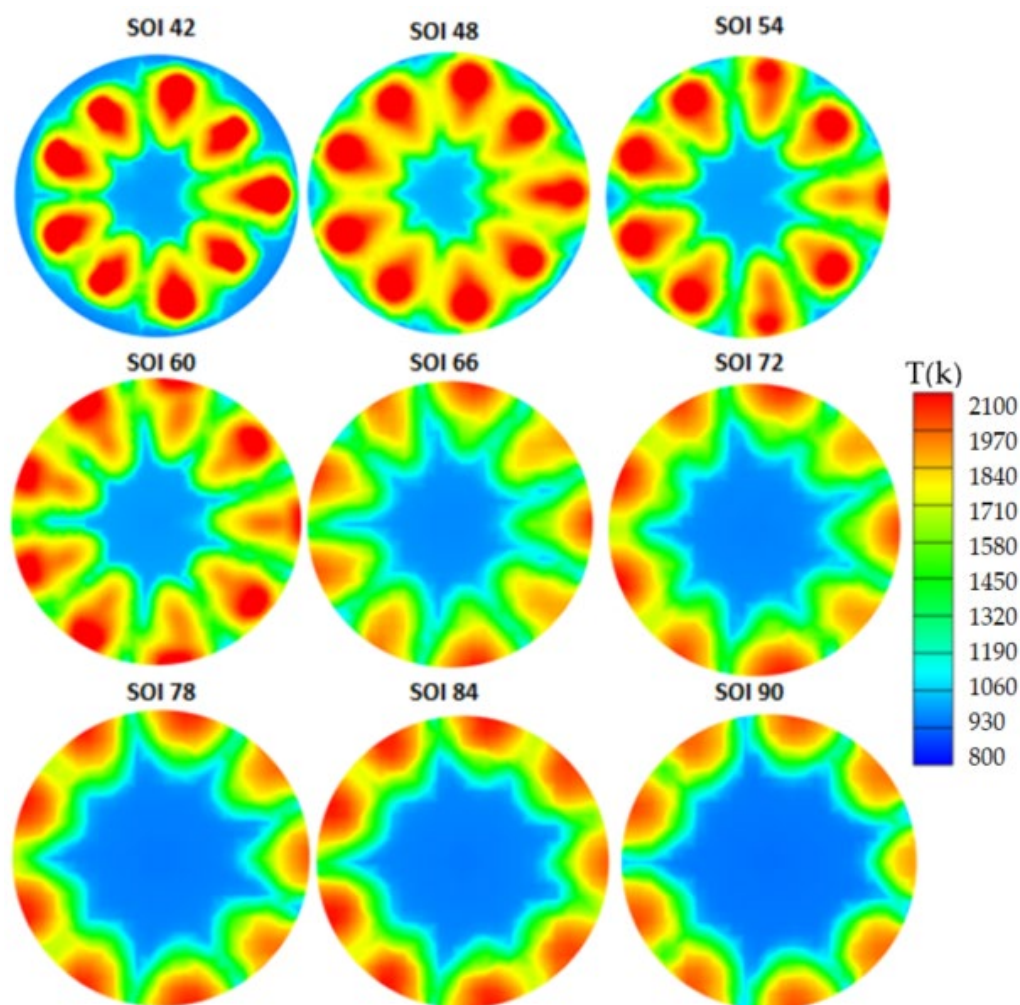


**Figure 15.** In cylinder temperature distribution at 4-degree aTDC (approx. CA50) in various injection timing.

Figure 16 represents the cylinder equivalence ratio at 4 CAD aTDC for injection timing case studies. The aim of illustrating this contour was to show the direct relation of high temperature zones to concentration of HRF fuel in the mixture. Case to case comparison with Figure 16 illustrated this relativity that shown the importance of mixture homogeneity to control temperature and flame propagation. It should be noted that high temperature zones were the spots that mainly produce  $\text{NO}_x$  emissions. THC as unburned hydrocarbon also released in too lean spots or void spot of HRF.

Combustion tracing was carried out to demonstrate hydrogen oxide (OH) concentrations with various crank angle degrees; see Figure 17. For this study, three injection timing cases, SOI 42, 54 and 66, were selected. OH concentration was shown in  $-5, 0, 5$  and  $10$  CAD aTDC. Importance of mixture homogeneity was obvious also in this figure. In all three-injection timings combustion has been started from rich zones of cylinder. In SOI 42 at  $-5$  CAD aTDC combustion mainly started from center area where the majority of HRF located at that area. Flame then propagated in the entire cylinder to any area that there was enough fuel to burn.

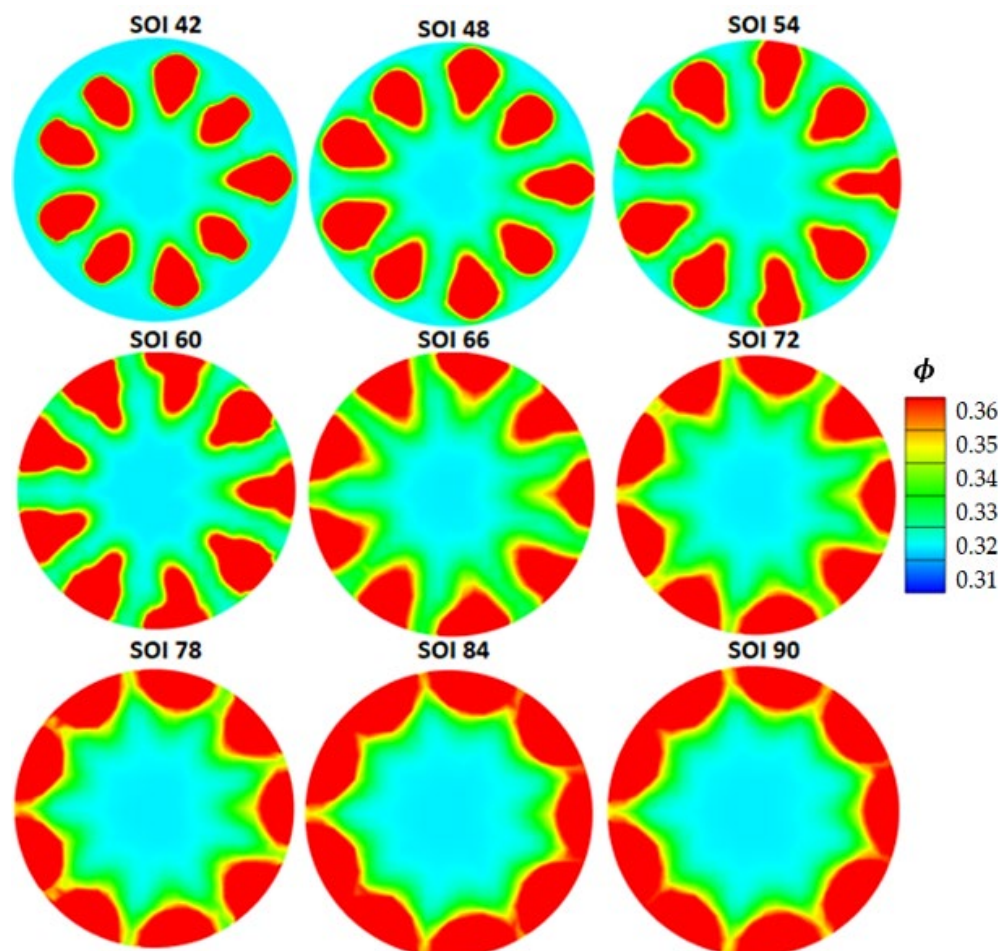


Figure 16. In-cylinder equivalence ratio, a section from top for all case studies at 4 CAD aTDC.

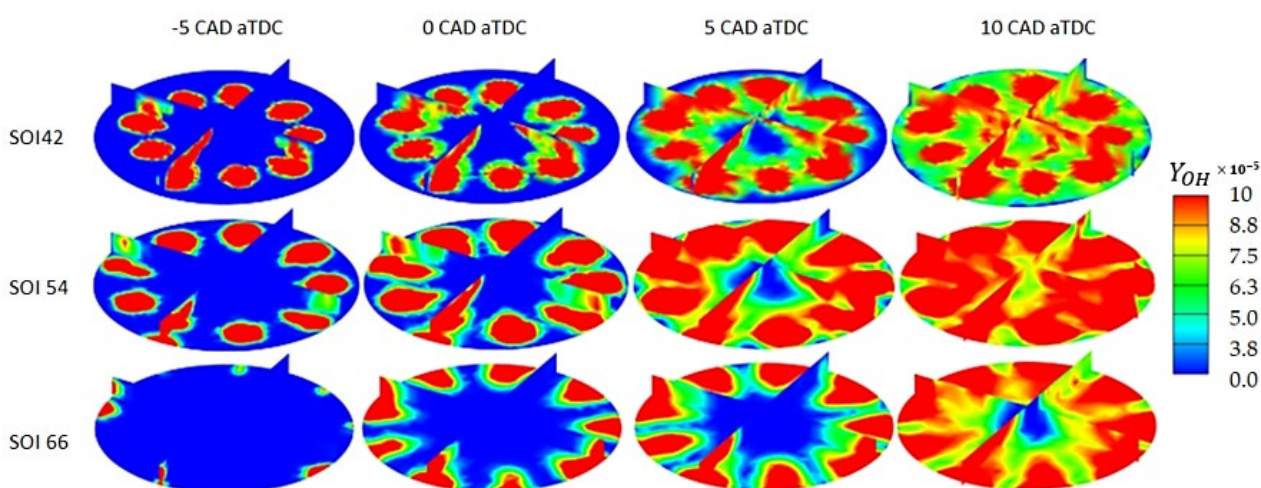
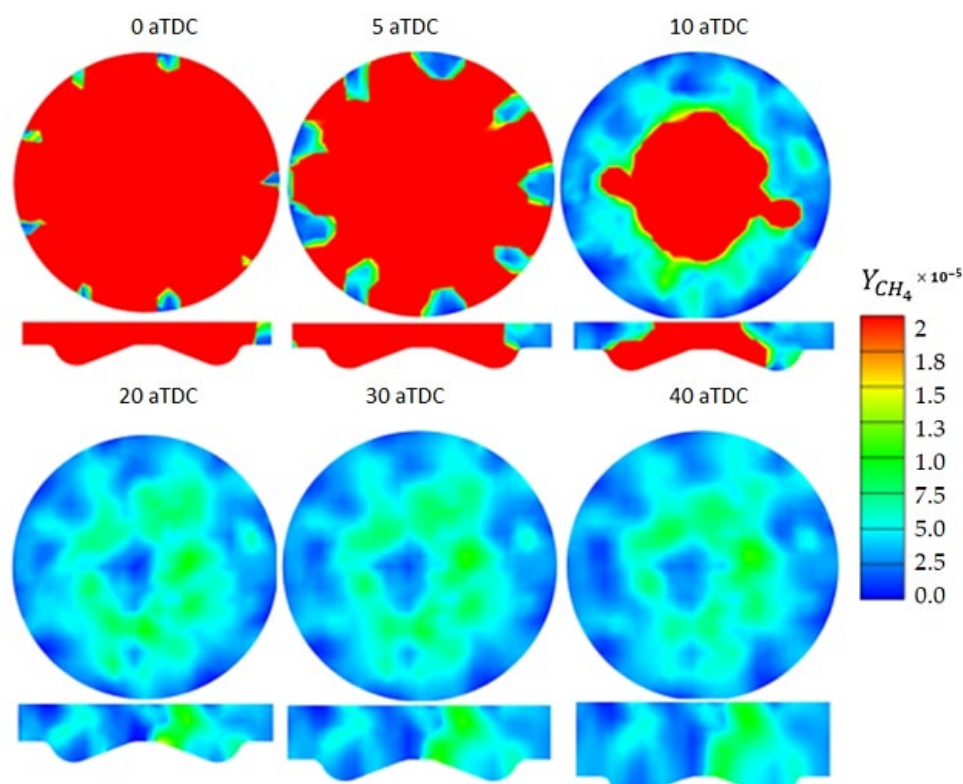


Figure 17. OH concentration for various injection timing in different crank angle degrees.

This situation also occurred for other cases, illustrated in Figure 17. For early injection combustion started approximately close to cylinder liner, propagated from that area to another spots of cylinder. Among these three cases, SOI 54 shown better flame spread than others but cannot considered as optimum due to higher level of  $\text{NO}_x$  production; see Figure 9. As a result, the ideal condition was to have a high level of homogeneity in center of the cylinder even in late injection cases.

Unburned hydrocarbon or THC is considered as main pollutant in RCCI engines which was a type of low temperature combustion (LTC) strategies. Here in this study to trace spots those contains higher amounts of THC,  $\text{CH}_4$  mass fraction was illustrated for SOI 66 in various CAD. Figure 18 illustrates the top and side view sections of  $\text{CH}_4$  mass fraction distributed in the cylinder in various CADs.



**Figure 18.**  $\text{CH}_4$  mass fraction distributed in the cylinder for SOI 66 at various engine crank angles.

Starting from top dead center (0 CAD),  $\text{CH}_4$  initially resided in the cylinder as low-reactivity fuel introduced through the intake port. As combustion initiated from the cylinder's rich zones (typically close to the liner in this case),  $\text{CH}_4$  consumption commenced in these areas. The consumption of  $\text{CH}_4$  gradually spread throughout the cylinder due to the propagation of the combustion flame towards the central and rich zones. As expected, the primary accumulation of unburned  $\text{CH}_4$ , or total hydrocarbons, concentrated in the central regions of the cylinder. It is worth noting that the study did not consider crevice geometry in its analysis.

#### 4. Conclusions

In this research, a numerical CFD modeling of a RCCI engine was conducted. The simulation process began with geometry and mesh generation, followed by the selection of a chemical kinetic mechanism (SK54) and liquid fuel properties that closely resemble the characteristics of LFO. Boundary conditions and initial values defined, and combustion modeling coupled with turbulence simulation captured complex combustion phenomena. Injector modeling and parcel configuration ensure realistic fuel injection simulations. Grid control and simulation parameters stroke a balance between computational efficiency and accuracy. Validation against experimental data was performed, with a focus on in-cylinder pressure and heat release rate. The tuned mechanism demonstrated significant improvements in predictions of engine specifications.

Visualizations of fuel distribution using local equivalence ratios have demonstrated that advancing the start of injection (SOI) increases mixture homogeneity up to a certain point, beyond which no further benefits are observed. Although in the case of higher

homogeneity, the voided area was also noticeable. A more homogeneous mixture at SOI 66 has been linked to improved emission outcomes, suggested that achieving optimal mixture homogeneity was crucial for enhancing overall emission performance in this particular study.

Higher in-cylinder temperatures were associated with late injection timings have been observed to increase the consumption of hydrocarbons, while as it was expected higher amounts of NO<sub>x</sub> produced. In addition to the general achievements, some more specific results are listed below:

Analyzing the spatial distribution of HRF with injection timing reveals that, a larger proportion of fuel mass is located close to liner for early SOI, i.e.,  $\geq 54$  CAD bTDC. However, for injection later than this value, the fuel distribution is increasingly located towards the cylinder axis.

Later injection timing causes high localized in-cylinder temperature zones approaching >2000 K. This causes NO<sub>x</sub> emissions to be greater than 100 times baseline value. At SOI of 66CAD bTDC, cylinder-out NO<sub>x</sub> below Euro V is attainable.

High in-cylinder temperatures consume higher amounts of hydrocarbons in late injection strategies. At SOI of 96CAD bTDC the amounts of THC have been obtained again more than 100 times greater than THC at early SOI of 42 CAD bTDC injection angle.

Late injection cases show higher IMEP. As such, maximum IMEP was obtained for an injection timing of 48 CAD bTDC

Visualization on fuel distribution with local equivalence ratio illustrates that advancing SOI leads to reduced levels of spatial inhomogeneity. This effect however levels off beyond injection timings of 80 CAD bTDC.

**Author Contributions:** Methodology, A.K. and M.M.; Software, A.K.; Validation, A.K.; Investigation, A.K.; Writing—original draft, A.K.; Writing—review & editing, M.M., A.V., M.A., M.M.S. and A.M.A.; Supervision, M.M., J.H. and A.M.A. All authors have read and agreed to the published version of the manuscript.

**Funding:** The work was conducted in the framework of the Clean Propulsion Technologies project with financial support from Business Finland (ref. 38475/31/2020).

**Data Availability Statement:** The data presented in this study are available on request from the corresponding author. The data are not publicly available due to limitations brought by Non Discloser agreement with Wärtsilä company as industrial partner.

**Conflicts of Interest:** The authors declare no conflict of interest. Authors Martin Axelsson and Jari Hyvönen were employed by the company Wärtsilä. The remaining authors declare that the research was conducted in the absence of any commercial or financial relationships that could be construed as a potential conflict of interest.

## Abbreviations

RCCI	Reactivity Controlled Compression Ignition
NO <sub>x</sub>	Nitrogen Oxides
iNO <sub>x</sub>	indicated Nitrogen Oxides
CAD	Crank Angle Degrees
SOI	Start of Injection
CFD	Computational Fluid Dynamics
HCCI	Homogeneous Charge Compression Ignition
PM	Particulate Matter
HC	Hydrocarbon
CO	Carbon Monoxide
CO <sub>2</sub>	Carbon Dioxide
IMEP	Indicated Mean Effective Pressure
CEM	Chemical Equilibrium Method
PDF	Probability Density Function
IVC	Intake Valve Close

EGR	Exhaust Gas Recirculation
THC	Total Unburned Hydrocarbons
iTHC	indicated Total Unburned Hydrocarbons
RANS	Reynolds-Averaged Navier–Stokes
MFB	Mass Fraction Burned
HRF	High-Reactivity Fuel
CA50	Crank Angle at 50% energy released
CA10	Crank Angle at 10% energy released
CA90	Crank Angle at 90% energy released
MZM	Multi-Zone Model
GT-Power	Engine Performance Simulation Software
RNG	Re-Normalization Group
O <sub>2</sub>	Oxygen
N <sub>2</sub>	Nitrogen
CAFE	Corporate Average Fuel Economy
COV	Coefficient of Variation
BD	Burn Duration
OH	Hydroxyl Radical
GRI	Gas Research Institute
LFO	Light Fuel Oil
SAGE	Semi-Analytical Green’s Function for Emission and Absorption
RIF	Radiation Interaction Factor
HOV	Heat of vaporization
RANS	Reynolds-averaged Navier-Stokes
RNG	Re-Normalization Group
TKE	Turbulent Kinetic Energy
KH	Kelvin–Helmholtz
RT	Rayleigh–Taylor

## References

- Li, J.; Yang, W.; Zhou, D. Review on the management of RCCI engines. *Renew. Sustain. Energy Rev.* **2017**, *69*, 65–79. [\[CrossRef\]](#)
- Reitz, R.D.; Duraisamy, G. Review of high efficiency and clean reactivity controlled compression ignition (RCCI) combustion in internal combustion engines. *Prog. Energy Combust. Sci.* **2015**, *46*, 12–71. [\[CrossRef\]](#)
- Benajes, J.; Novella, R.; Pastor, J.M.; Hernández-López, A.; Hasegawa, M.; Tsuji, N.; Emi, M.; Uehara, I.; Martorell, J.; Alonso, M. Optimization of the combustion system of a medium duty direct injection diesel engine by combining CFD modeling with experimental validation. *Energy Convers. Manag.* **2016**, *110*, 212–229. [\[CrossRef\]](#)
- Benajes, J.; Pastor, J.V.; García, A.; Boronat, V. A RCCI operational limits assessment in a medium duty compression ignition engine using an adapted compression ratio. *Energy Convers. Manag.* **2016**, *126*, 497–508. [\[CrossRef\]](#)
- Benajes, J.; García, A.; Pastor, J.M.; Monsalve-Serrano, J. Effects of piston bowl geometry on Reactivity Controlled Compression Ignition heat transfer and combustion losses at different engine loads. *Energy* **2016**, *98*, 64–77. [\[CrossRef\]](#)
- Liu, X.; Zhong, W.; Jiang, P.; Dai, L.; He, Z.; Wang, Q. Optimizing RCCI combustion for improved engine performance under low load conditions: Impact of low-reactivity fuel and direct injection timing. *Fuel* **2023**, *351*, 128871. [\[CrossRef\]](#)
- Wang, Y.; Zhu, Z.; Yao, M.; Li, T.; Zhang, W.; Zheng, Z. An investigation into the RCCI engine operation under low load and its achievable operational range at different engine speeds. *Energy Convers. Manag.* **2016**, *124*, 399–413. [\[CrossRef\]](#)
- Kakaee, A.-H.; Rahnama, P.; Paykani, A. Influence of fuel composition on combustion and emissions characteristics of natural gas/diesel RCCI engine. *J. Nat. Gas Sci. Eng.* **2015**, *25*, 58–65. [\[CrossRef\]](#)
- Molina, S.; García, A.; Pastor, J.M.; Belarte, E.; Balloul, I. Operating range extension of RCCI combustion concept from low to full load in a heavy-duty engine. *Appl. Energy* **2015**, *143*, 211–227. [\[CrossRef\]](#)
- Moradi, J.; Gharehghani, A.; Aghahasani, M. Application of machine learning to optimize the combustion characteristics of RCCI engine over wide load range. *Fuel* **2022**, *324*, 124494. [\[CrossRef\]](#)
- Loyte, A.; Suryawanshi, J.; Bhiogade, G.; Devarajan, Y.; Thandavamoorthy, R.; Mishra, R.; Natrayan, L. Influence of injection strategies on ignition patterns of RCCI combustion engine fuelled with hydrogen enriched natural gas. *Environ. Res.* **2023**, *234*, 116537. [\[CrossRef\]](#) [\[PubMed\]](#)
- Wang, L.; Liu, J.; Ji, Q.; Sun, P.; Li, J.; Wei, M.; Liu, S. Experimental study on the high load extension of PODE/methanol RCCI combustion mode with optimized injection strategy. *Fuel* **2022**, *314*, 122726. [\[CrossRef\]](#)
- Bilgili, L. A systematic review on the acceptance of alternative marine fuels. *Renew. Sustain. Energy Rev.* **2023**, *182*, 113367. [\[CrossRef\]](#)
- Valera-Medina, A.; Xiao, H.; Owen-Jones, M.; David, W.I.F.; Bowen, P.J. Ammonia for power. *Prog. Energy Combust. Sci.* **2018**, *69*, 63–102. [\[CrossRef\]](#)

15. Reiter, A.J.; Kong, S.-C. Combustion and emissions characteristics of compression-ignition engine using dual ammonia-diesel fuel. *Fuel* **2011**, *90*, 87–97. [[CrossRef](#)]
16. Yousefi, A.; Guo, H.; Dev, S.; Liko, B.; Lafrance, S. Effects of ammonia energy fraction and diesel injection timing on combustion and emissions of an ammonia/diesel dual-fuel engine. *Fuel* **2022**, *314*, 122723. [[CrossRef](#)]
17. Shen, Y.; Zhang, K.; Duwig, C. Investigation of wet ammonia combustion characteristics using LES with finite-rate chemistry. *Fuel* **2022**, *311*, 122422. [[CrossRef](#)]
18. Ganesan, N.; Viswanathan, K.; Karthic, S.V.; Ekambaram, P.; Wu, W.; Vo, D.-V.N. Split injection strategies based RCCI combustion analysis with waste cooking oil biofuel and methanol in an open ECU assisted CRDI engine. *Fuel* **2022**, *319*, 123710. [[CrossRef](#)]
19. Thomas, J.J.; Nagarajan, G.; Sabu, V.R.; Manojkumar, C.V.; Sharma, V. Performance and emissions of hexanol-biodiesel fuelled RCCI engine with double injection strategies. *Energy* **2022**, *253*, 124069. [[CrossRef](#)]
20. Madihi, R.; Pourfallah, M.; Gholinia, M.; Armin, M.; Ghadi, A.Z. Thermofluids analysis of combustion, emissions, and energy in a biodiesel (C<sub>11</sub>H<sub>22</sub>O<sub>2</sub>)/natural gas heavy-duty engine with RCCI mode (Part I: Single/two-stage injection). *Int. J. Thermofluids* **2022**, *16*, 100227. [[CrossRef](#)]
21. Madihi, R.; Pourfallah, M.; Gholinia, M.; Armin, M.; Ghadi, A.Z. Thermofluids analysis of combustion, emissions, and energy in a biodiesel (C<sub>11</sub>H<sub>22</sub>O<sub>2</sub>)/natural gas heavy-duty engine with RCCI mode (Part II: Fuel injection time/Fuel injection rate). *Int. J. Thermofluids* **2022**, *16*, 100200. [[CrossRef](#)]
22. Li, J.; Yang, W.M.; Goh, T.N.; An, H.; Maghbouli, A. Study on RCCI (reactivity controlled compression ignition) engine by means of statistical experimental design. *Energy* **2014**, *78*, 777–787. [[CrossRef](#)]
23. Li, J.; Yang, W.M.; An, H.; Zhao, D. Effects of fuel ratio and injection timing on gasoline/biodiesel fueled RCCI engine: A modeling study. *Appl. Energy* **2015**, *155*, 59–67. [[CrossRef](#)]
24. Fakhari, A.H.; Gharehghani, A.; Salahi, M.M.; Mahmoudzadeh Andwari, A.; Mikulski, M.; Hunicz, J.; Könnö, J. Numerical Investigation of Ammonia-Diesel Fuelled Engine Operated in RCCI Mode. In Proceedings of the 16th International Conference on Engines & Vehicles, Capri, Italy, 10–14 September 2023. SAE Technical Paper 2023-24-0057.
25. Ma, S.; Zheng, Z.; Liu, H.; Zhang, Q.; Yao, M. Experimental investigation of the effects of diesel injection strategy on gasoline/diesel dual-fuel combustion. *Appl. Energy* **2013**, *109*, 202–212. [[CrossRef](#)]
26. Nazemi, M.; Shahbakhti, M. Modeling and analysis of fuel injection parameters for combustion and performance of an RCCI engine. *Appl. Energy* **2016**, *165*, 135–150. [[CrossRef](#)]
27. Gharehghani, A.; Kakoe, A.; Andwari, A.M.; Megaritis, T.; Pesyridis, A. Numerical Investigation of an RCCI Engine Fueled with Natural Gas/Dimethyl-Ether in Various Injection Strategies. *Energies* **2021**, *14*, 1638. [[CrossRef](#)]
28. Nemati, A.; Ong, J.C.; Pang, K.M.; Mayer, S.; Walther, J.H. A numerical study of the influence of pilot fuel injection timing on combustion and emission formation under two-stroke dual-fuel marine engine-like conditions. *Fuel* **2022**, *312*, 122651. [[CrossRef](#)]
29. Yao, T.; Pei, Y.; Zhong, B.-J.; Som, S.; Lu, T.; Luo, K.H. A compact skeletal mechanism for n-dodecane with optimized semi-global low-temperature chemistry for diesel engine simulations. *Fuel* **2017**, *191*, 339–349. [[CrossRef](#)]
30. Vasudev, A.; Mikulski, M.; Balakrishnan, P.R.; Storm, X.; Hunicz, J. Thermo-kinetic multi-zone modelling of low temperature combustion engines. *Prog. Energy Combust. Sci.* **2022**, *91*, 100998. [[CrossRef](#)]
31. ISO 8217; FUEL STANDARD, Specifies the Requirements for Fuels for Use in Marine Diesel Engines and Boilers, Miami, FL, USA. 2017. Available online: <https://www.iso.org/obp/ui/en/#iso:std:iso:8217:ed-6:v1:en> (accessed on 8 May 2024).
32. Vasudev, A.; Cafari, A.; Axelsson, M.; Mikulski, M.; Hyvonen, J. Towards Next Generation Control-Oriented Thermo-Kinetic Model for Reactivity Controlled Compression Ignition Marine Engines. In *SAE Powertrains, Fuels & Lubricants Conference & Exhibition*; SAE Technical Paper 2022-01-1033; SAE: Warrendale, PA, USA, 2022.
33. Kakoe, A.; Vasudev, A.; Smulter, B.; Hyvonen, J.; Mikulski, M. A Predictive 1D Modeling Framework for Reactivity-Controlled Compression Ignition Engines, via a Chemistry-Based, Multizone Combustion Object. In Proceedings of the 16th International Conference on Engines & Vehicles, Capri, Italy, 10–14 September 2023; SAE International: Capri, Italy, 2023; p. 11.
34. Heywood, J.B. *Internal Combustion Engine Fundamentals*; McGraw Hill: New York, NY, USA, 1988.
35. *Convergent Science*; Version 3.1; Converge Manual; Convergent Science: Madison, WI, USA, 2023.
36. Jafari, B.; Seddiq, M.; Mirsalim, S.M. Impacts of diesel injection timing and syngas fuel composition in a heavy-duty RCCI engine. *Energy Convers. Manag.* **2021**, *247*, 114759. [[CrossRef](#)]
37. Ramesh, N.; Mallikarjuna, J.M. Evaluation of in-cylinder mixture homogeneity in a diesel HCCI engine—A CFD analysis. *Eng. Sci. Technol. Int. J.* **2016**, *19*, 917–925. [[CrossRef](#)]
38. Kang, Y.; Li, X.; Shen, H.; Chen, Y.; Liu, D.; Chang, J. Effects of combustion chamber diameter on the performance and fuel–air mixing of a double swirl combustion system in a diesel engine. *Fuel* **2022**, *324*, 124392. [[CrossRef](#)]
39. Singh, A.P.; Kumar, V.; Agarwal, A.K. Evaluation of comparative engine combustion, performance and emission characteristics of low temperature combustion (PCCI and RCCI) modes. *Appl. Energy* **2020**, *278*, 115644. [[CrossRef](#)]
40. Žvar Baškovič, U.; Vihar, R.; Rodman Oprešnik, S.; Seljak, T.; Ktrašnik, T. RCCI combustion with renewable fuel mix—Tailoring operating parameters to minimize exhaust emissions. *Fuel* **2022**, *311*, 122590. [[CrossRef](#)]

**Disclaimer/Publisher’s Note:** The statements, opinions and data contained in all publications are solely those of the individual author(s) and contributor(s) and not of MDPI and/or the editor(s). MDPI and/or the editor(s) disclaim responsibility for any injury to people or property resulting from any ideas, methods, instructions or products referred to in the content.